Does hygrothermal degradation of Mode I fatigue delamination resistance in carbon fibre reinforced polymer laminates depend on the ageing conditions?

Yao, Liaojun; Wei, Jingchao; He, Zixian; He, Yonglyu; Lomov, Stepan V.; Alderliesten, Rene C.

DOI
10.1016/j.compstruct.2024.118240

Publication date
2024

Document Version
Final published version

Published in
Composite Structures

Citation (APA)
Yao, L., Wei, J., He, Z., He, Y., Lomov, S. V., & Alderliesten, R. C. (2024). Does hygrothermal degradation of Mode I fatigue delamination resistance in carbon fibre reinforced polymer laminates depend on the ageing conditions? *Composite Structures*, *342*, Article 118240. https://doi.org/10.1016/j.compstruct.2024.118240

A Morphing Quadrotor-Blimp With Balloon Failure Resilience for Mobile Ecological Sensing

Suryansh Sharma, Mike Verhoeff, Floor Joosen, RR. Venkatesha Prasad, and Salua Hamaza

***Abstract*—The increasing popularity of helium-assisted blimps for extended monitoring or data collection applications is hindered by a critical limitation – single-point failure when the balloon malfunctions or bursts. To address this, we introduce Janus, a hybrid blimp-drone platform equipped with integrated balloon failure detection and recovery capability. Janus employs a triggered mechanism that seamlessly transitions the platform from a blimp to a standard quad-rotor drone. Utilizing multiple sensors and fusing their readings, we have developed a robust balloon failure detection system. Janus demonstrates omnidirectional mobility in blimp mode and transitions promptly into quadrotor mode upon receiving the signal. Our results affirm the successful recovery of the system from balloon failure, with a rapid response time of 66 ms to balloon failure detection. The drone morphs into a quadrotor and achieves recovery within 0.362 seconds in 90% of cases. By amalgamating the enduring flight capabilities of blimps with the agility of quad-rotors within a morphing platform like Janus, we cater to applications demanding both prolonged flight duration and enhanced agility.**

***Index Terms*—Blimps, ecology monitoring, failure resilience, morphing drones, remote sensing, UAV design.**

I. Introduction

HELIUM-ASSISTED aerial vehicles have experienced a resurgence in recent years [1]. High endurance aerial platforms facilitate various ecological applications, aerial sensing, surveillance and tracking [2], [3], [4], [5], [6]. Despite their longer operational times compared to multi-rotors and fixed-wing aircraft, these vehicles often sacrifice maneuverability [7].

Blimps, valued for their extended operation indoors and outdoors, are effective for data collection in vast terrains such as mountainous areas and forests, where endurance plays a key role. However, they are often under-actuated and lack lift generation capability, relying on a single point of failure –the balloon– which renders them unsuitable for environments with a high risk of balloon bursting. While research on failure-resistant multi-rotors and VTOLs is extensive [8], [9], [10], [11], [12], minimal attention has been given to the design of failure-resistant blimps. Besides the risk of accidental balloon failure leading to a crash, blimps used for wildlife monitoring or surveillance face deliberate targeting and compromise due to their large size, and thus vulnerability. Existing low-altitude blimps typically feature a single chamber balloon made of materials like Mylar, PVC, or latex, making them susceptible to intentional damage [13], [14], [15], [16], [17]. Thus, low-altitude aerial ecology monitoring requires a small and lightweight drone design. Materials like coated latex that prevent helium from escaping and offer lightweight alternatives suitable for such missions, while large-sized balloons become less maneuverable and more vulnerable to direct targeting.

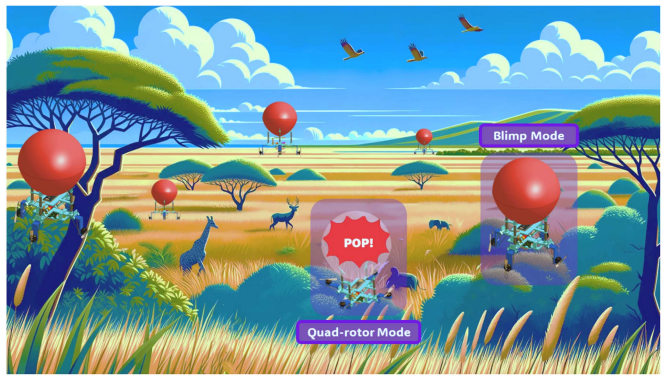

Fig. 1. *Janus* drone can fly like an omnidirectional helium-driven blimp and swiftly transition to a quadrotor in the event of a balloon failure. This versatility enables prolonged wildlife monitoring in areas vulnerable to poachers targeting the blimp.

To address the challenges above, we propose *Janus*, a hybrid quadrotor-blimp platform with built-in balloon failure detection and recovery capabilities (Fig. 1). Our design includes a mechanism that, when triggered, transitions the platform from a blimp to a quadrotor drone with minimal additional weight, limiting its impact on the blimp's balloon size. Building upon the planar blimp design BEAVIS [18], *Janus* utilizes four rotors attached to a helium-inflated balloon for increased manoeuvrability, agility, and extended operational air time compared to regular multi-rotor drones. Unlike a regular quadrotor, when in blimp mode the motors' axes lay in the horizontal plane i.e., propeller blades are vertical to the ground allowing for complete planar motion; additionally, the drone can also fly vertically making it omnidirectional.

In *Janus* [video-link], the four rotors swivel by 90° when the balloon fails, morphing the platform into a regular quadrotor drone in free fall. In the event of unintentional or intentional detachment of the balloon, the platform enters free fall, providing a brief window for reaction. To ensure a successful

Manuscript received 5 February 2024; accepted 15 May 2024. Date of publication 28 May 2024; date of current version 5 June 2024. This letter was recommended for publication by Associate Editor M. Wilfried Mueller and Editor G. Loianno upon evaluation of the reviewers' comments. *(Corresponding author: Suryansh Sharma.)*

Suryansh Sharma, Mike Verhoeff, Floor Joosen, and RR. Venkatesha Prasad are with the Networked Systems, Faculty of Electrical Engineering, Mathematics and Computer Science, Delft University of Technology, 2628 Delft, The Netherlands (e-mail: suryansh.sharma@tudelft.nl; m.verhoeff-2@tudelft.nl; f.e.joosen@tudelft.nl; r.r.venkateshaprasad@tudelft.nl).

Salua Hamaza is with the Biomorphic Intelligence Lab, Department of Control & Operations, Faculty of Aerospace Engineering, Delft University of Technology, 2628 Delft, The Netherlands (e-mail: s.hamaza@tudelft.nl).

Digital Object Identifier 10.1109/LRA.2024.3406061

transition without crashing, we implement a sensing algorithm to precisely detect the moment the balloon fails by exploring various sensing modalities, their response times, and a sensor fusion algorithm. Upon transitioning to quadrotor mode, the drone experiences gravitational acceleration during free fall, and the attitude of the drone becomes unpredictable after the balloon bursts. To address this, we devise a nonlinear geometric controller that stabilizes the platform, compensating for the large reaction force resulting from the balloon bursting.

Our contributions include the design of a resilient omni-directional blimp capable of transitioning into a regular quadrotor drone thanks to a novel morphing mechanism (Section II). We then present a balloon failure sensing algorithm utilizing sensor fusion for precise bursting detection, applicable to other blimps and balloon-based aerial vehicles (Section III). Additionally, we develop a nonlinear geometric flight controller for post-balloon failure recovery and subsequent quadrotor operation (Section IV). Results demonstrate the successful recovery of our system from balloon failure. The sensing algorithm detects balloon failure within 66 ms and triggers the transition. The performance evaluation of the transition mechanism exhibits a 100% success rate in 10 different balloon failure trials, with the drone transforming into a quadrotor within 0.36 s.

II. Morphing Drone Design

In blimp mode, the drone functions as an omni-directional blimp with four vertically angled motors for planar motion, attached to a large helium balloon for lift. Horizontal translation is controlled by individual motors, while altitude adjustments are made by regulating pressure at the centre of the airframe. The unique 90° motor rotations enable omni-directional flight with just one active motor. Our novel design, with horizontally placed motors, facilitates steering in 3D space, creating unexpected aerodynamic effects at the airframe centre that control vertical motion: all four motors spinning raise altitude by generating high pressure, while two opposite motors spinning create a low-pressure region, lowering altitude. Our system can leverage this aerodynamic flow interaction, as in *BEAVIS* [18], and utilize thrust vectoring from the four motors by adjusting their tilt angle, adding extra motion to the system without additional actuators. Such a motor arrangement significantly augments drone agility and maneuverability, affording the same degrees of freedom as a standard quadrotor. Despite a tenfold increase in battery life, balloon-induced drag does decrease the platform's speed.

In the event of balloon failure in this configuration, an unavoidable crash ensues, as the drone lacks the means to generate lift. A morphing mechanism is employed to switch the platform's motors into a configuration resembling a regular quadrotor. Activated by this mechanism, the platform transitions from blimp to quadrotor mode when triggered (Fig. 2). This entails a 90° clockwise swing of the motor arms, which latch in the horizontal position, aligning the motors in the horizontal plane to generate lift for flight.

The transition mechanism relies on constrained rotary joints connecting each motor arm to the platform body (Fig. 3). Each motor arm has a 90° freedom to rotate, and two rubber strips, serving as elastic forces, constantly attempt to return the motor arm to the stable horizontal position (quadrotor mode). The arms are interconnected via a rigid fishing line, facilitating their downward rotation into a vertical position (blimp mode) when tension in the line counters the pull of the rubber strips.

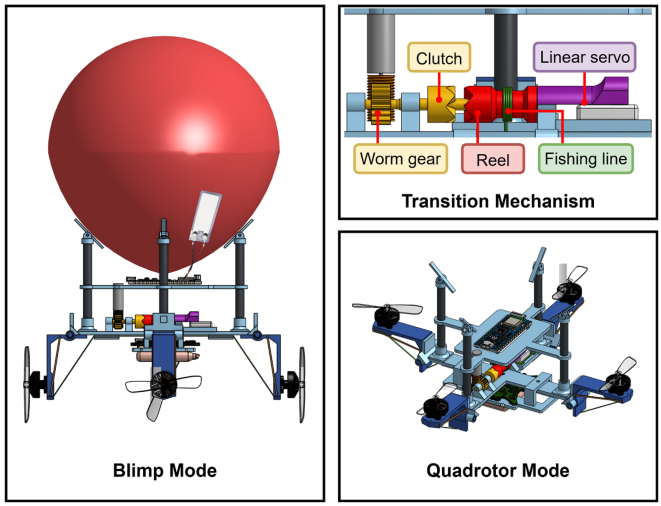

Fig. 2. *Janus* can morph between two modes: a blimp and a quadrotor, using a specially designed transition mechanism.

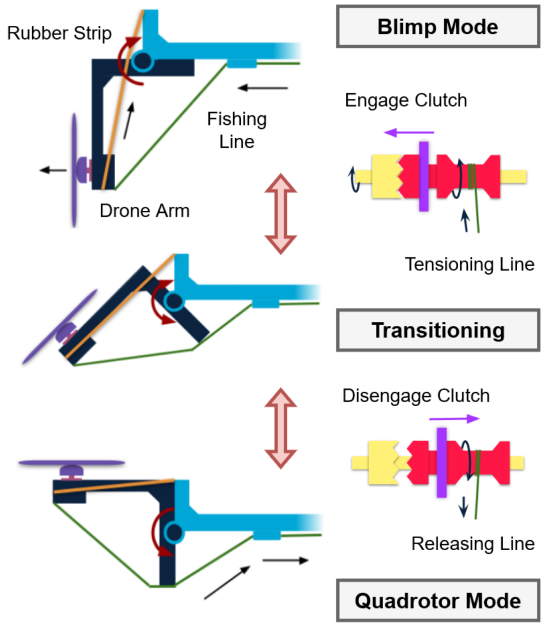

Fig. 3. *Janus* morphing mechanism transitions the blimp into a regular quadrotor via a reel and clutch system.

Tension on the fishing line is manipulated by a reel with an integrated clutch. A 6 mm 3 V DC coreless wind-up motor with a planetary gearbox drives the reel. The motor incorporates a worm gear attached to its shaft, enabling rotation in a single direction. The drone can disable the motor while maintaining tension in the line and release tension by uncoupling the motor and the reel using a linear servo.

The system includes a provision for recovering from an erroneous failure detection alarm. If the system mistakenly signals a balloon failure while the balloon is still intact, the transition mechanism is triggered, bringing the drone into quadrotor mode. Once the failure sensing system confirms that the alarm was a false positive, the drone can transition back to blimp mode using

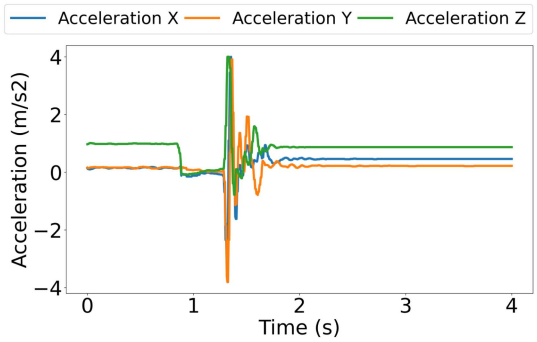

Fig. 4. Measured x, y, z accelerations when *Janus* drone is dropped from an altitude of 0.8 m.

the worm gear and the DC motor, facilitating recovery from false positive failure scenarios.

III. Sensing Balloon Failure

A. Sensing Requirements

Understanding the blimp-drone's operating environment is crucial as it greatly affects its failure sensing needs. Blimps, using helium for lift, are designed for fair weather and are easily diverted by strong winds, traveling slowly (e.g., BEAVIS had a max speed of 2.5 m/s indoors). They may encounter obstacles like trees and operate in cluttered and noisy environments like forests. Given these factors, specific requirements for a failure sensing system include:

1) Accurate detection: the system must precisely identify balloon failure leading to bursting, excluding partial failures like slow gas leakage. It needs high accuracy and robustness against false positives.
2) Rapid response: the sensing suite should minimize response time to ease the mechanical transition into a quadrotor. Delayed detection complicates stabilization of the quadrotor.
3) Low power and weight: as the platform transitions into a quadrotor, payload capacity decreases. With a finite battery, the drone needs a lightweight, low-power detection system for sustained quadrotor operation.

To underscore the significance of rapid and accurate detection, consider the scenario where the *Janus* platform is dropped from a height of 0.8 m and x, y, z acceleration are recorded (Fig. 4). The drone takes approximately 0.4 s to crash to the ground. During the interval of 0.9 to 1.3 s, the drone is in free fall, with the second spike indicating the impact with the ground. A longer sensing time results in accelerated platform movement, posing greater challenges to stabilize the system before a crash. Therefore, a limit for detecting failure is set at 0.391 s, corresponding to a drop of approximately 0.75 m, serving as an upper-bound for sensor selection.

B. Sensor Suite Design and Experimental Setup

Various sensors were evaluated based on requirements for the balloon failure system (Table I). The selection criteria consider the sensors' ability to detect specific physical parameters during and after balloon failure. For instance, a microphone can promptly detect the sound of the balloon bursting, but accuracy may be compromised by nearby loud noises. Investigating the sound frequency could help mitigate false positives. Alternatively, a proximity sensor using infrared light reflections can detect the presence of the balloon surface, but accuracy depends on detection precision and optimal mounting. Another consideration is using a piezoelectric sensor to detect strain on the balloon's surface, though it's vulnerable to false positives from platform collisions. Placement on the balloon surface is crucial for reliability. Mechanical options, like a pressure switch engaged by balloon pressure, are considered, but reliability diminishes due to potential misfires during collisions. After balloon failure, the platform experiences free fall and rotation, detectable by an accelerometer, yet susceptibility to false positives from collisions or descending platform must be addressed. Gyroscopes, while detecting rotation changes, are unreliable in predicting drone rotation during balloon failure and were excluded from further experimentation. Subsequent experiments focus on the microphone, proximity sensor, piezoelectric sensor, and accelerometer.

TABLE I
Possible Sensors for Detecting Balloon Failure

Sensor	Sensed parameter	Sensing time	Reliability
Acoustic Sensor	Balloon Bursting sound	Fast	Low
Accelerometer Sensor	Linear acceleration	Slow	Medium
Gyroscope Sensor	Angular velocity	Slow	Low
Mechanical Switch	Balloon pressure	Fast	Medium
Piezoelectric Sensor	Balloon surface strain	Fast	Medium
Proximity Sensor	Balloon surface reflection	Fast	High

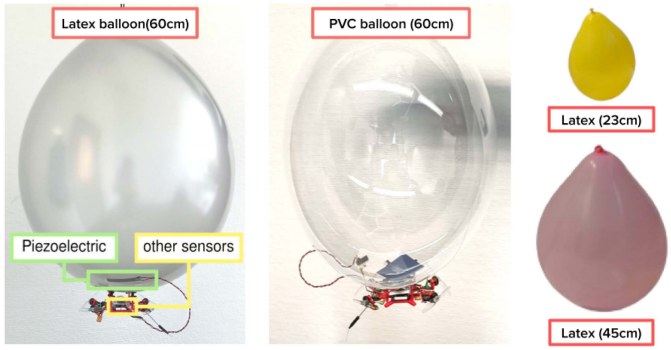

Fig. 5. Experimental setup with 60 cm latex balloon (left) and PVC balloon (middle). The piezo sensor is attached to the balloon surface, the other sensors are mounted between the platform and the balloon. Additional testing was carried out with 23 and 45 cm latex balloons (right).

The sensing algorithm runs on an Arduino Nano 33 BLE Sense microcontroller, utilizing sensors including an MP34DT06JTR microphone, an APDS9960 proximity sensor, a BMI270 accelerometer, and single-poled TE Connectivity piezoelectric films with a thickness of 205 µm. Experimentation involved 30 different balloons of 60, 45 and 23 cm diameter balloons placed on the *Janus* platform, with each sensor individually tested for detecting true positives by bursting the balloon. Both latex and PVC balloon were used (Fig. 5). The platform was tested with motors spinning at 50% PWM and for static hovering.

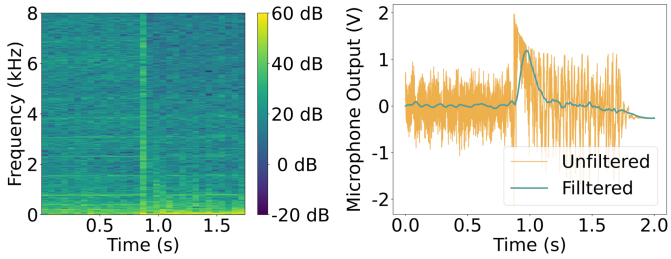

Fig. 6. Audio spectrogram (left) and temporal filtered signal (right) when blimp balloon bursts.

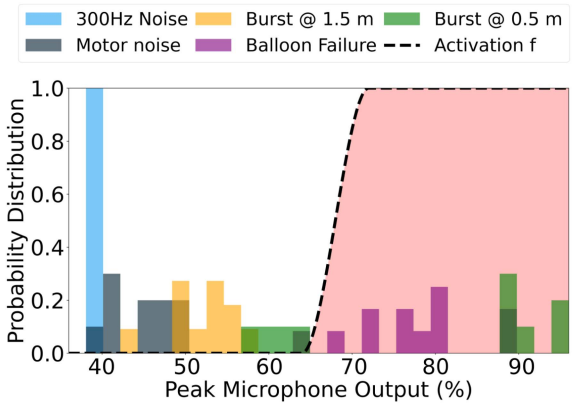

Fig. 7. The distribution of filtered peak microphone output recorded for different noise sources: stationary drone with motors spinning (grey), a 300 Hz constant noice tone (blue), balloon failure (purple), latex balloon popping at 0.5 m distance (green) and 1.5 m distance (yellow).

Response time was evaluated by recording video at 240 frames per second, with an onboard LED illuminating upon balloon burst detection. The difference between the first frame of balloon burst and the first illuminated frame was measured, achieving a resolution of 4 ms, meeting experimental requirements.

C. Acoustic Sensor

Sensor Setup: A low-power omni-directional, MEMS microphone sampled at 16 KHz, employing Fast-Fourier Transform is used to characterize noise and signal frequencies. A spectrogram of the balloon bursting sound, showcasing its spread across the entire spectrum(Fig. 6). The microphone, even while monitoring a specific frequency for balloon popping, picks up all high amplitude noises. A first-order Butterworth filter with a 5 Hz cutoff frequency mitigates this, preserving the balloon burst peak while eliminating rotor noise. The filtered signal's peak amplitude serves as a metric for balloon failure detection.

Sensor Performance: Fig. 7 shows multiple evaluated scenarios. The microphone is susceptible to broadband loud noise sources, but it effectively filters out narrowband noise sources. The most challenging scenario involved potential false detection when a balloon bursts in close proximity to the platform. Experiments involved bursting rubber latex balloons at distances of 50 cm and 150 cm from the platform, simulated this challenging scenario. The 300 Hz tone noise is completely filtered out, while the filtered sound of the motors exhibits a low amplitude. The latex balloon burst sound generates a high peak. However, the system is unable to distinguish this from other balloons bursting in close proximity. Furthermore, PVC balloons did not produce a loud burst and instead slowly lost air with a low amplitude hissing sound. Thus, the use of microphones is not well suited for the task of failure detection.

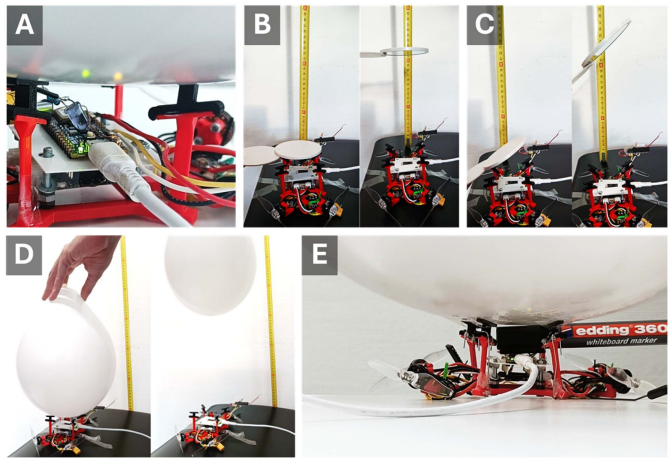

Fig. 8. False positive scenarios considered with a proximity sensor: (a) IR LED, (b) horizontal mirror, (c) 45 ° angled mirror, (d) different coloured balloons and (E) swiping different reflective objects like marker cap.

D. Proximity Sensor

Sensor Setup: The APDS9960 sensor detects proximity by measuring the infra-red light reflected from the surface of objects upto 10 cm away. The sensor output scales with increasing proximity to the balloon surface. Its placement is thus, crucial as it cannot be positioned too far. It was mounted at a distance of 5 cm between the platform and the balloon. However, potential false positives may arise from this gap when objects like tree branches get lodged. Furthermore, the proximity sensor's vulnerability to factors like balloon color, opacity, material as well as the presence of nearby reflective surfaces were taken into account when experimenting.

Several false positive sources were evaluated to test sensor performance (Fig. 8). An IR LED was used to test potential interference with the proximity sensor's functionality. Additionally, a mirror positioned at 0 and 45 degrees, was placed at 5 cm distance from the sensor and was moved to 15 cm in 2 s interval. This assessed if it had any potential effects on the sensor. Balloon color and material were also investigated using black, gray, white, blue, red, green, latex and transparent PVC balloons. Each balloon was moved them from 5 to 15 cm from the sensor. Finally, various reflective objects including a wooden, steel and plastic stick were lodged in the gap.

Sensor Performance: Fig. 9 consolidates the outcomes of these experiments. Colored latex balloons exhibited consistent sensor responses, with no significant differences between colors, and only one representative color is depicted in Fig. 9(a). Transparent PVC balloons behaved similarly, except when the bottom edge was pointed towards the proximity sensor, resulting in a peak. The mirror consistently maintained a high value for all cases. Fig. 9(b) illustrates the sensor's behavior during balloon failure, where a drop from 100 to 0 proximity is observed at 0.5 s. Drops at around 1.0 and 1.4 s may be attributed to pieces of the balloon momentarily blocking the sensor, with the

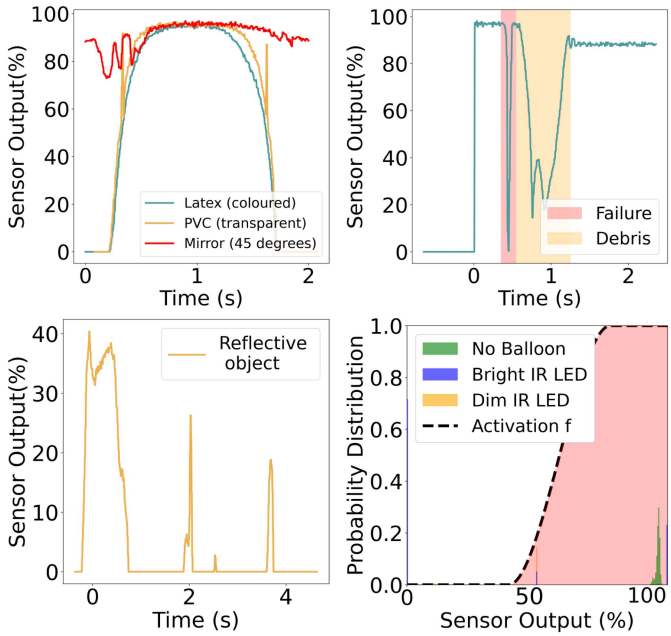

Fig. 9. Proximity sensor response when (a) coloured and transparent balloons are moved away from it, (b) blimp balloon fails (c) a reflective object like a marker cap is swiped in front of it and (d) an IR LED is shined next to to it.

value eventually settling at 85%. Fig. 9(c) portrays the effect of swiping an object in front of the proximity sensor, causing distortions in the value. The response to a wooden stick was distortion-free, while steel exhibited fewer but similar distortions. Fig. 9(d) demonstrates the influence of an IR LED on the proximity sensor, with bright and dim LEDs generating varying values depending on the presence or absence of the balloon. The sensor response time was within 4 ms.

E. Accelerometer

Sensor Setup: The accelerometer measures linear acceleration in x, y, z. Given that during balloon failure the platform experiences free fall, the output of this sensor is determined by the net magnitude of the resultant vector formed by these variables. This choice ensures functionality even if the accelerometer is oriented differently. Potential false positives may arise when the platform encounters collisions with objects, unrelated to balloon failure. Given that the drone would be deployed in forest areas, the accelerometer was tested by evaluating the impact of balloon collision with a tree trunk, branches and a small foam disk. The foam disk represented small seed or fruits which may fall on the balloon (Fig. 10). As a baseline, the accelerometer was also tested while the platform moved horizontally and vertically at a speed of 1 m/s. This aimed to evaluate if the blimp's motions alone could trigger false positives.

Sensor Performance: Fig. 11 (left) illustrates the impact of the platform's motion and balloon failure on accelerometer readings. In balloon failure experiments, the highest acceleration was 0.45 g, typically varying between 1 and 0.8 g. Measurements from the blimp's flight speed are presented, with an average accelerometer reading of 1 m/s^{-2} for both cases. Vertical movements ranged between 0.1 and 0.4 g, while lateral movements exhibited lower values between 0.05 and 0.2 g. When the platform

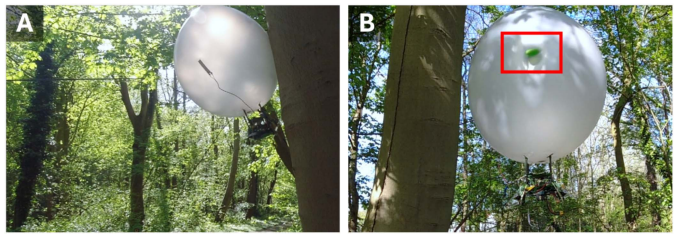

Fig. 10. *Janus* outdoor collision experiments with (A) a tree trunk and (B) a rubber disk emulating a small object.

was hovering with motors spinning, the vector length ranged between 0 and 0.05 g. The middle figure displays results from collision experiments, where the average acceleration measured was also 1 m/s^{-2}. For the branch and the small object, the minimum measured length ranged between 0 and 0.4 g, while the blimp hitting the trunk of a tree, resulting in a value of 0.6 g. The accelerometer response time was measured at 33 ms.

F. Piezoelectric Sensor

Sensor Setup: The piezoelectric sensor generates a voltage when its surface is distorted, with the output influenced by the parallel resistance used. A value of 100 KΩ was chosen to strike a balance between achieving a maximum peak value and minimizing noise. To mitigate interference, especially from disturbances to the balloon surface unrelated to failure, the sensor is positioned on the bottom side of the balloon (Fig. 5). This placement minimizes the risk of direct impact on the sensor in case of collisions with objects. While an alternative placement between the platform body and the balloon is possible, it may interfere with the proximity sensor's operation. The piezoelectric sensor is affixed using tape at the bottom and top to allow for optimal bending. Similar to the accelerometer, the piezoelectric sensor is sensitive to collisions, particularly direct hits. Collision experiments, previously conducted with the accelerometer, were replicated using the piezoelectric sensors, along with variations involving direct hits to the sensor or the side of the balloon.

Sensor performance: Fig. 11 illustrates collision experiments. When colliding with a tree the readings is less than 5% of full scale value. When the tree hits hits the blimp on the sensor side this value is between 0 and 10% and between 90 and 100% during balloon failure. Readings between 0 and 30% can be seen when the small object (rubber disk) hits the blimp's side but can vary upto 90% when the sensor was hit directly. This shows that the sensor is susceptible to false readings especially when directly hit. The piezoelectric sensor demonstrated a response time within 4 ms.

G. Balloon Failure Sensing Algorithm

From all evaluated sensors, the proximity, piezoelectric, and accelerometer show potential for measuring balloon failure. As previously indicated, the microphone can not accurately detect balloon failure when evaluating different balloon materials. For each sensor, a sigmoid function was developed. This serves to act as a threshold based activation function that is used to scale the output from each sensor to a failure detection probability. The upper and lower thresholds determine the range where there is no failure probability (0 or 1), and within this range,

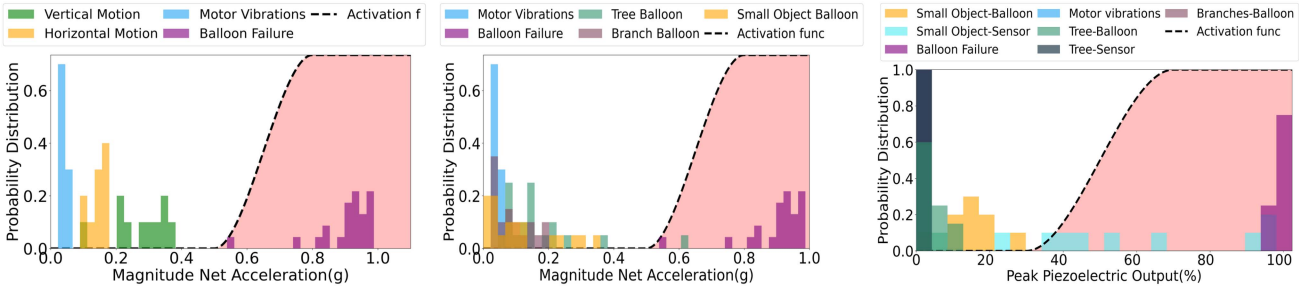

Fig. 11. The distribution of the accelerometer vector length when moving(left) and when colliding with different objects (middle) and the distribution of the peak piezoelectric sensor output when hit with small objects, tree and branches (right).

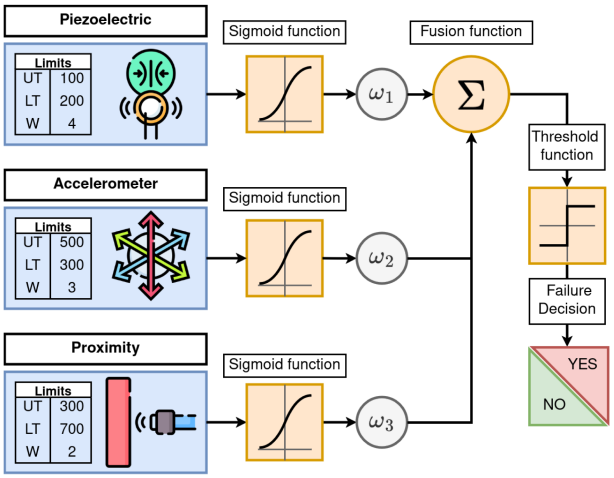

Fig. 12. Balloon failure sensing algorithm showing data flow as well as tunable weights, and upper and lower sigmoid thresholds used for each sensor to detect failure.

the probability scales from 0 to 1 using an approximation of the Sigmoid function. This output from the sigmoid function is then multiplied by a weight that was determined based on experimental data and is subject to the blimp construction. The weight essentially assigns a detection confidence to the output of each sensor. Different blimp designs can assign this based on prioritising different sensed physical parameters.

The outputs from individual sensor detection confidences are summed to produce a fused output value, which is then compared to a threshold value. In our setup this was found after extensive balloon failure testing to be 5.0. This comes from a study of different false positives as well sensor outputs under different balloon failure scenarios as described in previous subsections. If the fused output surpasses the threshold, the system identifies a balloon failure. The algorithm, thresholds and weights for the sensors are detailed in Fig 12. Among the assessed sensors, the proximity sensor stands out as the most promising in terms of detection accuracy. Potential false positives may involve objects becoming lodged in the gap between the drone and balloon or directing an IR LED precisely into the proximity sensor. Given the size of the gap, such occurrences are deemed improbable. Malicious intent would require close proximity to the blimp, where alternative methods to crash the blimp could already be employed. Moreover, the IR LED must be aimed directly at the proximity sensor, as bouncing light off the balloon surface will not activate it. A direct impact on the piezoelectric sensor during a collision can also lead to a false positive. The accelerometer, while less prone to the experimented false positives, may still register a single significant collision as a balloon burst. The sensor fusion approach thus, amalgamates the outputs from multiple sensors and thus enhances the overall reliability of the failure sensing system by pooling their outputs.

Our method determines threshold and weight values empirically but these are adjustable based on balloon and blimp characteristics. Values are presented for 60 cm latex balloons but can be updated for other balloon parameters. Sensor outputs are scaled relative to their full scale value to generalize the approach for different sensor models and deployment scenarios. In terms of sensing time, the accelerometer achieves 33 ms while the proximity and piezoelectric sensors are the fastest at 4 ms. All four sensors meet the required 0.39 s upper bound. The current setup is also adaptable to various helium reservoir designs with adjustments. Multiple proximity or piezoelectric sensors can be employed, each with independent thresholds and weights. Poly-reservoir designs can integrate these sensors into the existing sensing subsystem, with outputs added to the summation function. Empirical testing is necessary to set thresholds and weights, though not addressed in this study.

IV. Geometric Flight Controller

The flight control system aims to maintain a desired attitude if the balloon fails, as unpredictable forces can induce random accelerations. Upon balloon failure detection, the system triggers a transition mechanism, shifting the platform's operational mode from blimp to quadrotor. In quadrotor mode, the drone is in free fall with uncertain attitude, necessitating a control system to stabilize it before ground impact. Traditional control systems using Euler angles have limitations due to singularities, restricting complex rotational maneuvers. Given our system's potential random drone orientation requiring corrective maneuvers, we opt for a geometric control-based approach. Geometric control systems are suitable for dynamic systems on nonlinear manifolds not globally identified with Euclidean spaces [19].

Consider the quadrotor drone shown in Fig. 13. There exists an inertial reference frame $\{\vec{x}, \vec{y}, \vec{z}\}$ and a body-fixed frame $\{\vec{b}_1, \vec{b}_2, \vec{b}_3\}$. The i-th rotor generates a thrust f_i and a reaction torque τ_i along $-\vec{b}_3$ for $1 \leq i \leq 4$. The magnitude of the total thrust and the total moment in the body-fixed frame is denoted by $f, M \in \mathbb{R}^3$, respectively.

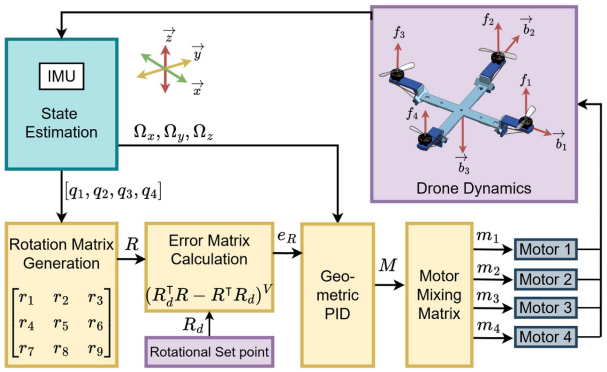

Fig. 13. Block diagram of the *Janus* geometric PID controller.

The drone configuration is defined by its attitude with respect to the inertial frame. Therefore, the configuration manifold is the Lie group called Special Euclidean SE(3), which is the semidirect product of $\mathbb{R}^3$ and the special orthogonal group $SO(3) = \{R \in \mathbb{R}^{3x3} \mid R^T R = I, detR = 1\}$. Fig. 13 also shows the block diagram of the geometric controller in *Janus*. Note the hat map, $\wedge : \mathbb{R}^3 \to SO(3)$ is defined by the condition that $x \wedge y = x \times y$ for all $x, y \in \mathbb{R}^3$. This identifies the Lie algebra SO(3) with $\mathbb{R}^3$ using the vector cross product in $\mathbb{R}^3$. The inverse of the hat map is denoted by the Vee map, $\vee : SO(3) \to \mathbb{R}^3$

We assume that the thrust of each propeller can be directly controlled, and the direction of this thrust is normal to the quadrotor plane. Propellers 1 and 3 rotate clockwise, and propellers 2 and 4 rotate counterclockwise. They all generate thrust along the direction of $-\vec{b}_3$. The thrust magnitude $f = \sum f_i$ is positive when the total thrust vector acts along $-\vec{b}_3$, and negative when the total thrust vector acts along $\vec{b}_3$. Using the definition of the rotation matrix $R \in SO(3)$, the total thrust vector is given by $-fRe_3 \in \mathbb{R}_3$ in the inertial frame. We also assume that the torque generated by each propeller is directly proportional to its thrust. The thrust of each propeller can be converted directly into f and M, or vice versa. The control system takes the thrust magnitude $f \in \mathbb{R}$ and the moment vector $M \in \mathbb{R}^3$ as control inputs. The thrust magnitude is taken directly as input from the user flying the drone or is kept constant. The moment vector M is used to stabilize the drone attitude.

We get the quaternion vector Q comprising of $[q_1, q_2, q_3, q_4]$ from the IMU of the drone which is then converted into a rotational matrix R using the following relation,

$$R = \begin{bmatrix} 2(q_1^2 + q_2^2) - 1 & 2(q_2q_3 - q_1q_4) & 2(q_2q_4 - q_1q_3) \\ 2(q_2q_3 - q_1q_4) & 2(q_1^2 + q_3^2) - 1 & 2(q_3q_4 - q_1q_2) \\ 2(q_2q_4 - q_1q_3) & 2(q_3q_4 - q_1q_2) & 2(q_1^2 + q_4^2) - 1 \end{bmatrix}. \tag{1}$$

The error vector e_R is computed via R_d, the rotational set point vector specifying the angle of rotation. In the default stabilisation case, $R_d = I$:

$$e_R = (R_d^\intercal R - R^\intercal R_d)^\vee. \tag{2}$$

The moment vector M can then be calculated using the error vector e_R and angular velocity vector Ω using the non-linear attitude controller shown below,

$$M = K_p e_R - K_d \Omega + K_i \int (e_R) dt + K_{d\Omega} \dot{\Omega}. \tag{3}$$

The control moment is composed of proportional, derivative, and integral terms along with a feed-forward term that uses $\dot{\Omega}$. The values of the constants K_p, K_d, K_i, and $K_{d\Omega}$ were found experimentally by mounting the drone on the Open Gimbal platform [20] shown in Table II. An emphasis was put in stabilizing x and y over yaw stabilization.

TABLE II
JANUS GEOMETRIC PID CONTROLLER TUNED PARAMETERS

Parameter	x	y	z
K_p	10000	10000	2000
K_d	1000	1000	200
K_i	1000	1000	1000
$K_{d\Omega}$	200	200	0

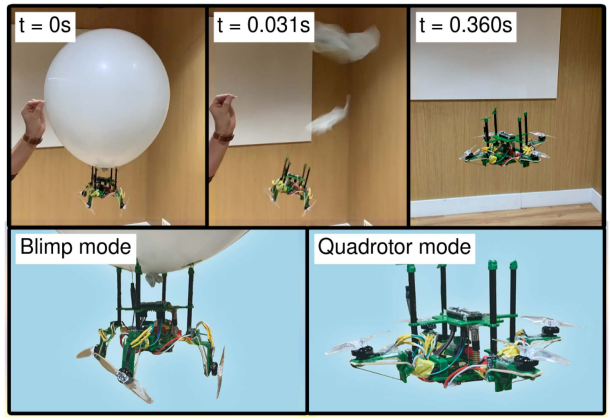

Fig. 14. *Janus* prototype in blimp mode sensing balloon failure and transitioning into quadrotor mode.

V. System Performance and Discussion

Drone prototypes were constructed using 3D-printed PLA frame, with 5 mm carbon fiber rods, and 60 cm and 90 cm helium-filled latex balloons. The platform, weighing 159 grams, featured 4 1202 brushless DC motors, a Crazyflie Bolt flight controller, and a 3000 mAh Li-ion battery. Balloon failure was induced by bursting the inflated balloon and recorded at 240 fps with an LED indicating the failure sensing result. Contact switches on each motor arm tracked orientation to estimate the transition mechanism's response time. Ten trials were conducted using the 60 cm and and five trials using the 90 cm balloons. In half of the 60 cm trials the drone hovered statically while in the other it translated horizontally.

Fig. 14 illustrates the drone's morphing process from blimp to quadrotor, depicting the initial blimp mode, balloon bursting, and the subsequent transition. A close-up of both modes is provided. Fig. 15 presents the fused sensor detection confidence with a threshold set at 5.0. Balloon failure detection was successful in all 15 repeats for both sizes of balloons and blimp motion, achieving a 100% accuracy rate. While the accelerometer and proximity sensor consistently sensed failure in all cases, the piezoelectric sensor exhibited degraded output due to continuous

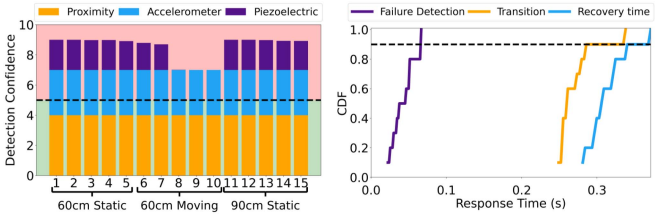

Fig. 15. Distribution of different sensors' detection confidence across balloon failure trials (left) and CDF plot of balloon failure sensing, transitioning and recovering time (right).

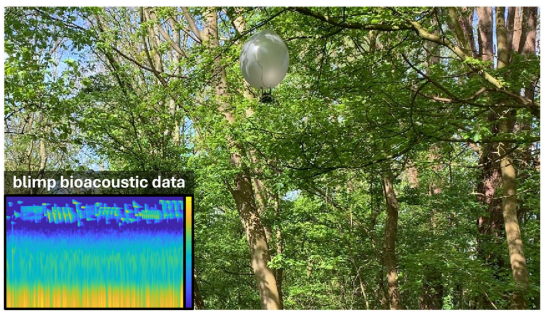

Fig. 16. *Janus* deployed in a forest to collect bioacoustic data.

impacts from the balloon, emphasizing the need for replacement after multiple balloon failure instances. Fig. 15 also illustrates the Cumulative Distribution Function (CDF) of the drone's transition time from blimp to quadrotor. In 90% of cases, the drone successfully morphs within 0.362 s after balloon failure. The average response time for failure detection is 0.038 s, with a standard deviation of 0.015 s, and the maximum observed sensing time is 0.066 s. *Janus* is designed for low-altitude sensing, complementing other drones for wildlife monitoring and data collection. While not intended to replace stratospheric airships or high altitude platforms, it can mitigate risks in outdoor deployments that originate from malicious and accidental sources. Fig. 16 depicts *Janus* collecting bio-acoustic data in a forest near trees. The platform's ability to hover silently presents a promising avenue for drone assisted ecology monitoring.

VI. Conclusion

We introduced *Janus*, a hybrid aerial platform suitable for mobile environmental sensing applications. Our design augments an omni-directional blimp, allowing it to transition into a regular quadrotor drone on command, or under necessity. A multiple sensor based balloon failure detection algorithm, developed to detect balloon failure within 66 ms, is discussed along with mechanical design methodology and system components. To enable in-flight transition, a geometric flight controller is designed to detect and react to balloon faults, adjusting the drone's attitude for continued safe flight. A prototype is built to assess performance, revealing a 90% probability of recovery from balloon failure within 0.36 s. Indoor and outdoor experimental validation with manual balloon failure induction confirmed the system's efficacy.

References

[1] M. Koziol, "The tech is finally good enough for an airship revival," Jan. 2023. [Online]. Available: https://spectrum.ieee.org/airship
[2] R. Saitou, Y. Ikeda, and Y. Oikawa, "Three-dimensional noise and spatial mapping system with aerial blimp robot," *Acoustical Sci. Technol.*, vol. 40, no. 1, pp. 12–22, 2019.
[3] N. Yao, E. Anaya, Q. Tao, S. Cho, H. Zheng, and F. Zhang, "Monocular vision-based human following on miniature robotic blimp," in *Proc. IEEE Int. Conf. Robot. Automat.*, 2017, pp. 3244–3249.
[4] W. Yamada, H. Manabe, and D. Ikeda, "ZeRONE: Safety drone with blade-free propulsion," in *Proc. Conf. Hum. Factors Comput. Syst.*, 2019, pp. 1–8.
[5] L. Zheng and S. Hamaza, "ALBERO: Agile landing on branches for environmental robotics operations," *IEEE Robot. Automat. Lett.*, vol. 9, no. 3, pp. 2845–2852, Mar. 2024.
[6] S. Hamaza, I. Georgilas, G. Heredia, A. Ollero, and T. Richardson, "Design, modeling, and control of an aerial manipulator for placement and retrieval of sensors in the environment," *J. Field Robot.*, vol. 37, no. 7, pp. 1224–1245, 2020.
[7] D. Palossi, A. Gomez, S. Draskovic, A. Marongiu, L. Thiele, and L. Benini, "Extending the lifetime of nano-blimps via dynamic motor control," *J. Signal Process. Syst.*, vol. 91, no. 3, pp. 339–361, 2019.
[8] S. Sun, G. Cioffi, C. d. Visser, and D. Scaramuzza, "Autonomous quadrotor flight despite rotor failure with onboard vision sensors: Frames versus events," *IEEE Robot. Automat. Lett.*, vol. 6, no. 2, pp. 580–587, Apr. 2021.
[9] C. J. Boss and V. Srivastava, "In-flight actuator failure recovery of a hexrotor via multiple models and extended high-gain observers," *IEEE Robot. Automat. Lett.*, vol. 6, no. 4, pp. 6204–6211, Oct. 2021.
[10] E. Baskaya, M. Hamandi, M. Bronz, and A. Franchi, "A novel robust hexarotor capable of static hovering in presence of propeller failure," *IEEE Robot. Automat. Lett.*, vol. 6, no. 2, pp. 4001–4008, Apr. 2021.
[11] S. J. Lee, I. Jang, and H. J. Kim, "Fail-safe flight of a fully-actuated quadrotor in a single motor failure," *IEEE Robot. Automat. Lett.*, vol. 5, no. 4, pp. 6403–6410, Oct. 2020.
[12] N. Gandhi, D. Saldaña, V. Kumar, and L. T. X. Phan, "Self-reconfiguration in response to faults in modular aerial systems," *IEEE Robot. Automat. Lett.*, vol. 5, no. 2, pp. 2522–2529, Apr. 2020.
[13] M. Burri et al., "Design and control of a spherical omnidirectional blimp," in *Proc. IEEE/RSJ Int. Conf. Intell. Robots Syst.*, 2013, pp. 1873–1879.
[14] H. Cheng, Z. Sha, Y. Zhu, and F. Zhang, "RGBlimp: Robotic gliding blimp - design, modeling, development, and aerodynamics analysis," *IEEE Robot. Automat. Lett.*, vol. 8, no. 11, pp. 7273–7280, Nov. 2023.
[15] J. Müller, N. Kohler, and W. Burgard, "Autonomous miniature blimp navigation with online motion planning and re-planning," in *Proc. IEEE/RSJ Int. Conf. Intell. Robots Syst.*, 2011, pp. 4941–4946.
[16] C. Lu et al., "A heterogeneous unmanned ground vehicle and blimp robot team for search and rescue using data-driven autonomy and communication-aware navigation," *Field Robot.*, vol. 2, pp. 557–594, 2022.
[17] H. Zhang and J. P. Ostrowski, "Visual servoing with dynamics: Control of an unmanned blimp," in *Proc. IEEE Int. Conf. Robot. Automat.*, 1999, pp. 618–623.
[18] S. Sharma et al., "BEAVIS: Balloon enabled aerial vehicle for IoT and sensing," in *Proc. 29th Annu. Int. Conf. Mobile Comput. Netw.*, 2023, pp. 1–15.
[19] F. Goodarzi, D. Lee, and T. Lee, "Geometric nonlinear PID control of a quadrotor UAV on SE(3)," in *Proc. Eur. Control Conf.*, 2013, pp. 3845–3850.
[20] S. Sharma, T. Dijkstra, and R. V. Prasad, "Open gimbal: A 3 degrees of freedom open source sensing and testing platform for nano and micro UAVs," *IEEE Sens. Lett.*, vol. 7, no. 9, Sep. 2023, Art. no. 2502704.